OPEN

Electronic structure, thermodynamic stability and high-temperature sensing properties of Er-α-SiAlON ceramics

Yuwaraj K. Kshetri[1]*, Takashi Kamiyama[2], Shuki Torii[2], Sang Hoon Jeong[3], Tae-Ho Kim[4], Heechae Choi[5], Jun Zhou[6], Yuan Ping Feng[6] & Soo Wohn Lee[1,3]*

α-SiAlON ceramics have been in use as engineering ceramics in the most arduous industrial environments such as molten metal handling, cutting tools, gas turbine engines, extrusion molds, thermocouple sheaths, protective cover for high-temperature sensors, etc., owing to their outstanding mechanical, thermal and chemical stability. Taking advantage of the intrinsic properties of α-SiAlONs, we investigate, in this paper, the possibility of using the Er-doped α-SiAlON (Er-α-SiAlON) ceramic as a high-temperature sensing material via its unique near-infrared to visible upconversion property. We first use neutron diffraction and density functional theory calculations to study the electronic structure and thermodynamic stability of Er-α-SiAlON. It is found that the interstitial doping of Er stabilizes the α-SiAlON structure via chemical bonds with O-atoms with N:O ratio of 5:2 in the seven-fold coordination sites of the Er^{3+} ion. Temperature-dependent upconversion emissions are then studied under 980 and 793 nm excitations over a temperature range of 298–1373 K and the fluorescence intensity ratio (FIR) technique has been employed to investigate the temperature sensing behavior. Temperature-dependent Raman behavior is also investigated. We demonstrate that using Er-α-SiAlON as a sensing material, the limit of temperature measurement via the FIR technique can be pushed well beyond 1200 K.

SiAlON ceramics are high-performance refractory ceramics which are manufactured by combining raw materials silicon nitride, alumina, aluminum nitride along with the oxide of rare earth elements. The SiAlON ceramics exist in two basic forms; each form is isostructural with one of the two common forms of Si_3N_4. In α-SiAlON, Si in the tetrahedral structure in Si_3N_4 is replaced by Al with limited substitution of N by O. Valancy requirements are satisfied by modifying cations occupying the interstitial holes at (1/3, 2/3, z) and (2/3, 1/3, ½ + z) per unit cell of the α-Si_3N_4[1]. In this way cations of yttrium (Y), calcium (Ca), lithium (Li), neodymium (Nd), Erbium (Er), etc., for example, can be incorporated into the structure. Consequently, α-SiAlON has the general formula $M_x^{v+}Si_{12-m-n}Al_{m+n}O_nN_{16-n}$ where x = m/v and M is the metal cation[1]. The interstitial dissolution of the M ion stabilizes the α-SiAlON structure and the cations M are coordinated by seven (N, O) atom sites[2,3].

α-SiAlON ceramics are widely used for high-temperature and high-endurance applications owing to their ability to withstand high structural loads and their excellent thermal and chemical stability[4,5]. Taking advantage of their superior mechanical, thermal and chemical stabilities, these materials have also been investigated recently for the possibility of functional applications such as downshifting phosphor materials for solid-state lighting[6]. In another aspect of investigating the functional properties of these ceramics, we recently reported efficient near-infrared to visible frequency upconversion in lanthanides (Ln^{3+})-doped α-SiAlON ceramics[7–9]. Er-doped α-SiAlON (Er-α-SiAlON) ceramic has moderately low phonon energy and can be a potential

[1]Research Center for Eco-Multifunctional Nano Materials, Sun Moon University, Chungnam, 31460, Republic of Korea. [2]Institute of Materials Structure Science, High Energy Accelerator Research Organization J-PARC Center, KEK, 203-1, Tokai, Ibaraki, 319-1106, Japan. [3]Department of Environment and Bio-Chemical Engineering, Sun Moon University, Chungnam, 31460, Republic of Korea. [4]Division of Mechanics and ICT Convergence Engineering, Sun Moon University, Chungnam, 31460, Republic of Korea. [5]Institute of Inorganic Chemistry, University of Cologne, 50939, Cologne, Germany. [6]Department of Physics, National University of Singapore, 2 Science Drive 3, 117551, Singapore, Singapore. *email: yuwarajkhatri@gmail.com; swlee@sunmoon.ac.kr

1

upconversion material for high-temperature applications. In one particular application, SiAlON ceramic has been used as protective ceramic coatings for sensing device protection and improving thin-film durability for long term high-temperature application at 1000 °C[10]. But the possibility of using the SiAlON ceramic itself as a high-temperature sensing material via its functional property has not been investigated so far.

It is known that Er^{3+} ion has a thermally coupled pair of energy levels $^2H_{11/2}$ and $^4S_{3/2}$, whose green emission intensity varies with temperature. By measuring the fluorescence intensity ratio (FIR) of the two green emission peaks from Er^{3+} ions, it is possible to use it as a probe for measuring environmental temperature where it is inserted[11–14]. The optical temperature sensing based on the FIR technique has attracted considerable attention for high sensitivity and accuracy of the measurement. However, the host materials for the optical temperature sensors are mainly based on glasses and fluorides[15–20]. These glass hosts have relatively poor stability which hampers their application as high-temperature sensors. Moreover, for glasses, the glass transition temperature must be taken into account because it marks the smooth passage of glass to the super-cooled molten state during heating. The glass transition region is the limiting parameter for the temperature range in which the glass temperature sensor can be applied[11]. For example, tellurite glass-based material cannot be used for temperature above 250 °C (523 K) due to its very low transition temperature (350 °C). To overcome these limitations, Er-α-SiAlON ceramic can be a potential candidate for the optical thermometry applications based on the FIR technique. A particular advantage of investigating the Er-α-Sialon as a high-temperature sensor material is that it has outstanding mechanical, thermal and chemical stability even at an elevated temperature above 1000 °C (1273 K)[4]. This offers a very high laser-induced damage threshold which in turn offers high spectral stability of the sensing material.

For the application of Er-α-SiAlON in a high-temperature environment, an understanding of its thermodynamic stability is also essential. In spite of the huge number of experimental investigations of α-SiAlON ceramics, only a few first principles calculations of Ca, Y, and Dy-doped α- and β-SiAlONs have been reported[21–23]. The structures of α-SiAlONs are complex and have not been precisely determined, because the random distribution of O and N leads to fluctuating bond lengths. Cole et al.[24] used the technique of extended X-ray absorption fine structure (EXAFS) spectroscopy in Er-α-SiAlON to investigate the local environment surrounding the Er^{3+} stabilizing cation. The work confirms the seven-fold coordination of the modifying cation within the interstices but indicates a N:O ratio of 5:2 rather than the 6:1 ratio as indicated by the Rietveld refinements of calcium and yttrium containing α-SiAlON by Izumi et al.[2,25]. X-ray diffraction technique is not sufficient because the scattering factors of both Si and Al and also O and N are too similar which prevents to obtain precise occupancy information. Similarly, EXAFS suffers the same issue of contrast and is difficult to implement when substitution concentration is low. In contrast to these techniques, neutron diffraction analysis is particularly appropriate to study the preferential occupation in SiAlONs because the lighter elements Si, Al, O and N have considerably different neutron scattering lengths. For example, neutron scattering lengths for O and N are 5.803 fm and 9.360 fm, respectively. Hence neutron diffraction of Er-α-SiAlON in conjunction with first principles calculation can provide greater insight into the local structure and high-temperature stability of this material.

In this work, we present a systematic investigation of thermodynamic stability and electronic structure of Er-α-SiAlON using density functional theory (DFT) calculations. We carried out neutron diffraction experiment to find accurate crystal structure for the electronic structure calculations. We then demonstrate the potential application of Er-α-SiAlON for high-temperature measurement in optical thermometry via the FIR technique. We also investigate the temperature dependence of the Raman spectra of Er-α-SiAlON which has not been reported for SiAlON-based materials.

Result and Discussion

Crystal structure from neutron diffraction. The Rietveld data fit on the neutron diffraction data of the Er-α-SiAlON ceramic and the difference pattern between simulated and the experimental data are shown in Fig. 1(c). α-SiAlON is the most dominant phase observed. A small amount of impurity phase was identified and was assigned to 12H-SiAlON polytypoids (less than 2%). In hot-press-sintered SiAlONs starting with α-Si_3N_4, a trace amount of β-SiAlON usually appears as an impurity phase. However, no β-SiAlON phase was observed in our system. The structural details of the Er-α-SiAlON ceramic as calculated by Rietveld refinement is shown in Supplementary Table S1 online. Taking into account the difference in composition between our sample and by Cao et al.[26], for the neutron diffraction, there is a good agreement in the lattice parameters and atomic positions. The refined crystal structure obtained from the neutron diffraction was used as starting geometry for the DFT calculations.

Thermodynamic stability and electronic structure. The formation energies of Er, Al and O doped systems were calculated for the chemical reactions below (reactions I to VI). The temperature was set to the sintering temperature of 1850 °C. Solid Er_2O_3 was considered as reservoirs of the Er^{3+} dopant in our modeling. The reactions of Al-O codoping, Er-O codoping, and Er-, O- doping are as follow:

(I) Substitution of Al-O co-doping (Al_{Si}-O_N)

$$\frac{x}{2}Al_2O_3 + Si_3N_4 \rightarrow Si_{3-x}Al_xN_{4-x}O_x + \frac{x}{4}O_{2(g)}\uparrow$$
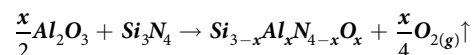
(II) Interstitial Al^{3+} formation with a triple positive charge (Al_{int}^{3+})

$$\frac{x}{2}Al_2O_3 + Si_3N_4 \rightarrow Si_3Al_xN_4 + \frac{3x}{4}O_{2(g)}\uparrow$$
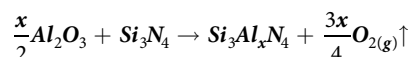
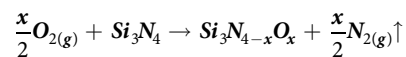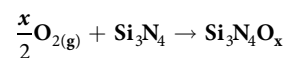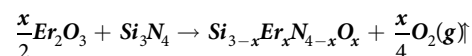(III) Substitution of O for N (O_N)
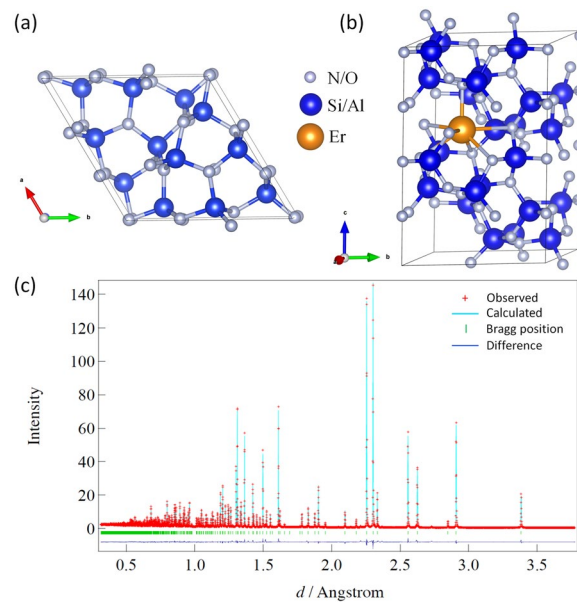
Figure 1. (**a**) Primitive unit cell of α-Si$_3$N$_4$ viewed along nearly parallel to c vector. (**b**) $1 \times 1 \times 2$ supercell of Er-α-SiAlON. (**c**) Neutron diffraction spectrum of Er-α-SiAlON ceramic.
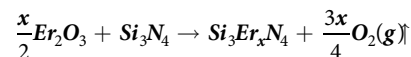
$$\frac{x}{2}O_{2(g)} + Si_3N_4 \rightarrow Si_3N_{4-x}O_x + \frac{x}{2}N_{2(g)}\uparrow$$

(IV) Interstitial O^{2-} formation with a double negative charge (O$_{int}^{2-}$)

$$\frac{x}{2}O_{2(g)} + Si_3N_4 \rightarrow Si_3N_4O_x$$

(V) Substitutional Er-O codoping (Er$_{Si}$-O$_N$)

$$\frac{x}{2}Er_2O_3 + Si_3N_4 \rightarrow Si_{3-x}Er_xN_{4-x}O_x + \frac{x}{4}O_2(g)\uparrow$$

(VI) Interstitial Er^{3+} formation with triple positive charge (Er$_{int}^{3+}$)

$$\frac{x}{2}Er_2O_3 + Si_3N_4 \rightarrow Si_3Er_xN_4 + \frac{3x}{4}O_2(g)\uparrow$$

The doping energies of the reactions considered above are plotted as a function of oxygen chemical potential in Fig. 2. The formation energy of interstitial Al-doping (Al$_{int}^{3+}$) was much higher than those of all the other doping reactions (5.4 eV/atom for the temperature of 1850 °C) and was not depicted in Fig. 2. It is seen that the substitutional Al-O codoping (Al$_{Si}$-O$_N$) is much stable than interstitial Al-doping (Al$_{int}^{3+}$), while Er-interstitial doping (Er$^{3+}_{int}$) is more stable than substitutional doping of Er along with adjacent O (Er$_{Si}$-O$_N$). From the calculated formation energies of Al-, O-, and Er-doping, the most stable configuration of Er-α-SiAlON is obtained by Al-O codoping in substitutional sites and Er^{3+} doping in the interstitial site. It is, therefore, evident that the interstitial doping of Er^{3+} ion, as shown in the model structure in Fig. 1(b), gives thermodynamically the most stable configuration of Er-α-SiAlON. This is in good agreement with the experimental observation that the doped metal cations in α-SiAlON take interstitial positions[1,25]. In the (Al/Si, O/N) doping the Al and O atoms prefer the nearest site (See Supplementary Fig. S1(a) online). In (Er/Si, O/N) substitution, Er and O atoms also prefer the nearest sites as shown in Supplementary Fig. S1(b) online, but this structure is highly unstable because of its higher formation energy (Er$_{Si}$-O$_N$) as can be seen from Fig. 2. In addition, neither interstitial O^{2-} doping (O$_{int}^{2-}$) nor substitutional O/N doping with one excess positive charge (O$_N^+$) is stable as shown in Fig. 2.

Since Er^{3+} doping into the interstitial site is energetically favorable and Er and O atoms prefer nearest sites, we calculated the formation energies of this configuration for a different number of O atoms surrounding the Er atom as shown in Fig. 3(a–d). The corresponding graph of the formation energies for varying oxygen chemical potential is shown in Fig. 3(e). We see that Er-α-SiAlON is highly stable especially with the atomic structure model shown in Fig. 3(c). That is, the Er-interstitial doping is highly stabilized via chemical bonding with two O-atoms doped in N-sites. This configuration leads to N:O ratio of 5:2 in the seven-fold coordination environment around Er^{3+} ion. This result is in good agreement with the experimental study by Cole et al.[24] of the local environment of the Er^{3+} stabilizing cation in Er-α-SiAlON. According to their work, Er^{3+} stabilizing cation has seven-fold coordination within the interstices but indicates a N:O ratio of 5:2 rather than the 6:1 ratio as indicated by the Rietveld refinements of calcium and yttrium containing α-SiAlON by Izumi et al.[2,25]. Hence, our
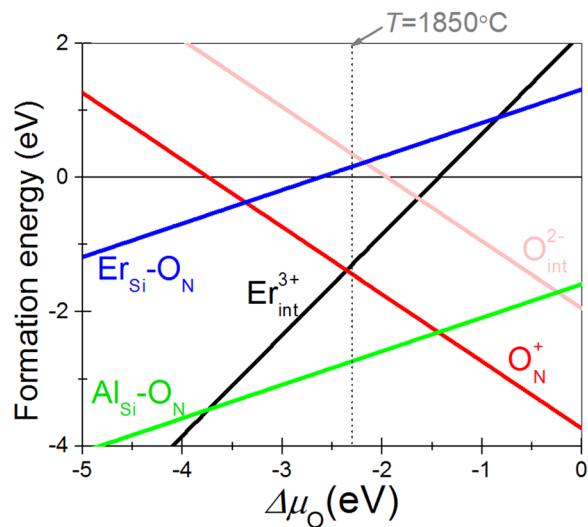
Figure 2. Calculated formation energies of Al-, O- and Er-doping in Si_3N_4. The dotted vertical line is consistent with the processing temperature of 1850 °C.
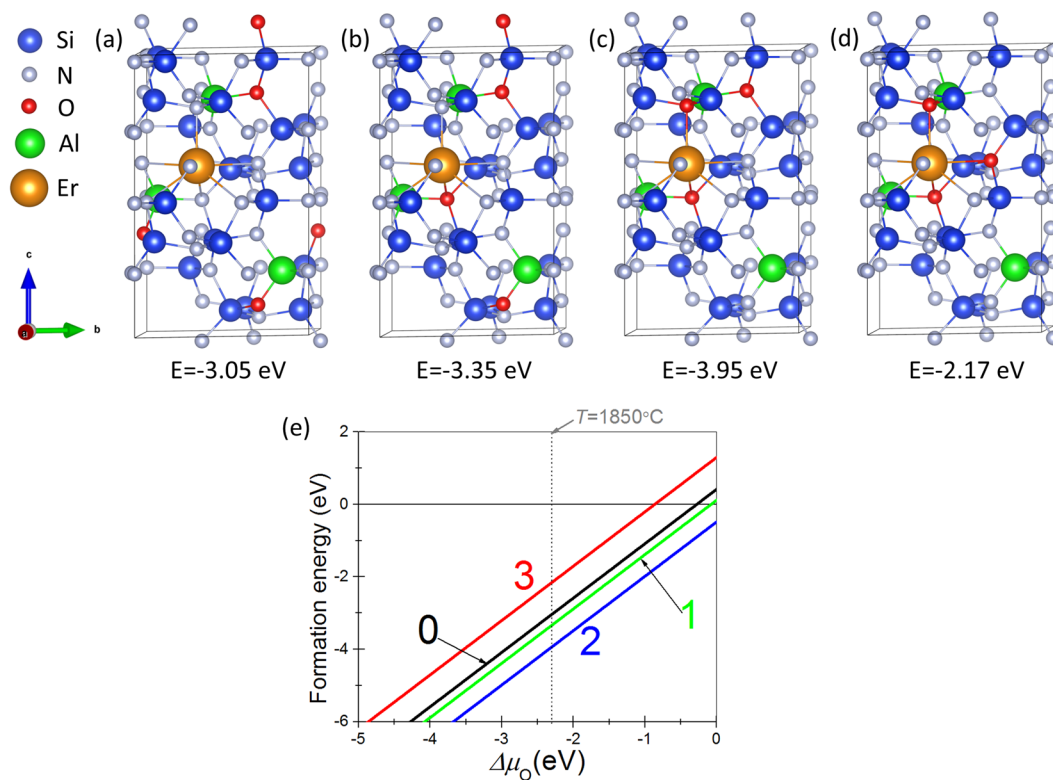

Figure 3. Number of Er–O bonds and formation energies; (**a**) no Er–O bonds, (**b**) one Er–O bond, (**c**) two Er–O bonds, and (**d**) three Er–O bonds, respectively. The model (**c**) is energetically the most stable configuration. (**e**) Formation energies for varying oxygen chemical potential. The curves labeled 0, 1, 2, and 3 correspond to the formation energy of model (**a**), (**b**), (**c**) and (**d**), respectively.

first principles calculation confirms that the stabilizing cation Er^{3+} does occupy the large closed interstices in the (Si, Al)–(N, O) network positioned at (0.333, 0.667, z) and (0.667, 0.333, 0.500 + z) with N:O ratio of 5:2 in the seven-fold coordination sites surrounding the stabilizing cation. Because of the small cation site, the metal cation evidently prefers coordination with smaller O anions than the larger N anions, as compared to that expected from average O/N ratio[27].

The calculated band gap of the pure Si_3N_4 is 4.7 eV, which is smaller than the experimental band gap of 5.1 eV of α-Si_3N_4[28]. It is well known that GGA underestimates the band gap. Kresse et al.[29] have predicted a much larger
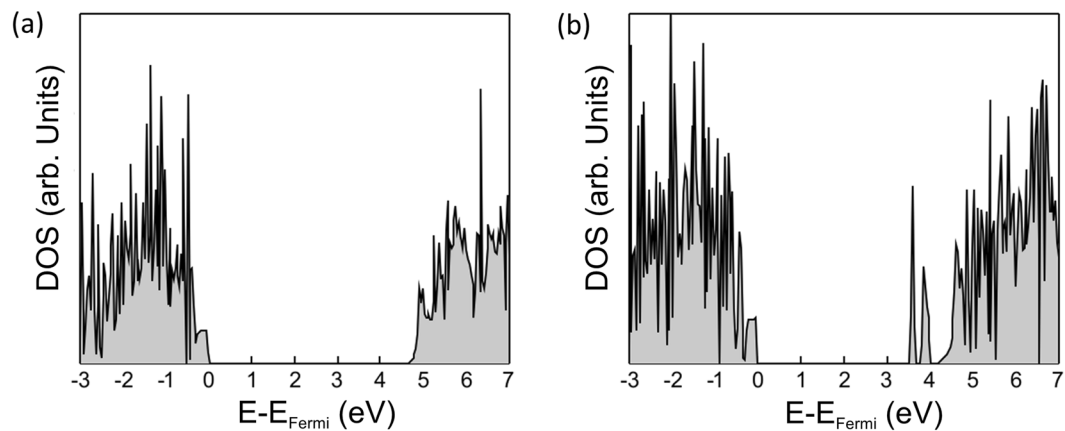
Figure 4. The electron density of states of (**a**) α-SiAlON and (**b**) Er-α-SiAlON, respectively.

band gap of 6.1 eV from self-consistent quasiparticle GW calculations. The density of states (DOS) of the most stable configuration of α-SiAlON and Er-α-SiAlON are shown in Fig. 4(a) and (b), respectively. The two mid-gap states below the conduction band emerge for the most stable configuration of Er-α-SiAlON while they are absent for the α-SiAlON. The mid-gap states in Er-α-SiAlON can, therefore, be attributed to the Er^{3+} ion. The band gap is also reduced to 4.22 eV. This reduction in band gap and the presence of the mid-gap states make Er-α-SiAlON an optically active material.

Microstructure investigation. The TEM micrograph in Fig. 5(a) reveals the grains of α-SiAlON phase in the sintered body. The lattice spacing calculated from the selected area electron diffraction (SAED) pattern, Fig. 5(b), which correspond to the lattice planes (210), (101) and (201) subsequently verifies the α-SiAlON phase. The energy dispersive spectroscopy (EDS) spectra 1 and 2 which correspond to the points inside the α-SiAlON grain indicate that the elemental distributions within different grains are fairly similar. The EDS spectrum 3 corresponding to the triple junction shows a relatively higher Er concentration. It is because in equilibrium situation during sintering, the Er^{3+} ions which cannot be incorporated into the α-SiAlON lattice may segregate in the triple junctions. The high-angle annular dark-field (HAADF) TEM image and corresponding elemental mappings show the homogeneous distribution of elements across the matrix of Er-α-SiAlON. The high-resolution TEM (HRTEM) image of the Er-α-SiAlON has been shown in Supplementary Fig. S2 online. A very thin grain boundary (less than 1 nm) can be seen which indicates effective incorporation of the sintering aids into the α-SiAlON lattice. The lattice spacing of 0.251 and 0.230 nm of the upper and lower grains in the HRTEM image correspond to (210) and (112) crystal planes, respectively, which are also consistent with the α-SiAlON phase.

Upconversion and temperature sensing property. Figure 6(a) shows the upconversion emission spectra of Er-α-SiAlON under 980 and 793 nm excitations measured at room temperature. It can be seen that emission intensity is stronger under 980 nm. The two strong green emission bands centered at 537 and 558 nm are attributed to $^2H_{11/2} \rightarrow {}^4I_{15/2}$ and $^4S_{3/2} \rightarrow {}^4I_{15/2}$ transitions while weak red emission band centered at 682 nm is assigned to $^4F_{9/2} \rightarrow {}^4I_{15/2}$ transition of Er^{3+}, respectively. For the temperature sensing property, the strong green emission bands are responsible. The pump power dependence of the emission intensity of each green emission band under 980 nm and 793 nm excitations has been shown in Fig. 6(b,c), respectively. Pollnau et al.[30] have shown that the emission intensity I is proportional to the nth power of the absorbed pump power P i. e., $I \propto P^n \Rightarrow \mathrm{Log}(I) \propto n\ \mathrm{Log}(P)$ where n is the number of pump photons absorbed per upconverted photon and is given by the slope of the emission intensity versus pump power in a double-logarithmic scale. As shown in Fig. 6(b,c) of the plots of the log I versus log P, the number of photons involved for the two green emission bands at 537 nm and 558 nm under 980 nm excitation are 1.3 and 1.7 while that under 793 nm excitation are 2.1 and 2.3, respectively. Hence, the upconversion mechanism under both laser excitations consists of a two-photon absorption process. Some deviation of n from typical values is due to the competition between the linear decay and the upconversion processes for the depletion of the intermediate excited states. Based on this observation, a schematic energy level diagram of Er^{3+} under both 980 and 793 nm excitations has been presented in Fig. 6(d). Two possible mechanisms are responsible for the upconversion emission, viz., ground state absorption (GSA) followed by excited state absorption (ESA) and energy transfer upconversion (ETU) under both the excitation wavelengths. The former involves only one optically active Er^{3+} ion successively promoted to the upper levels by the resonant absorption of two or more laser photons, whereas the latter is a many-body non-radiative mechanism involving two or more nearby interacting Er^{3+} ions. Both mechanisms can co-exist to effectively contribute to the population of the higher excited emitting level[17]. Detail, mechanism of the upconversion process has been investigated under 980 nm and ~800 nm by several researchers[31–33]. Under 980 nm excitation, two successive absorptions of photons bring electrons from the ground state $^4I_{15/2}$ to the $^4F_{7/2}$ excited state via the intermediate state $^4I_{11/2}$. The green-emitting states $^2H_{11/2}$ and $^4S_{3/2}$ are then populated by rapid non-radiative relaxations of $^4F_{7/2}$ level. Upon excitation by 793 nm laser, $^4I_{9/2}$ level is first excited and quasi-instantaneously the $^4I_{13/2}$ level is populated
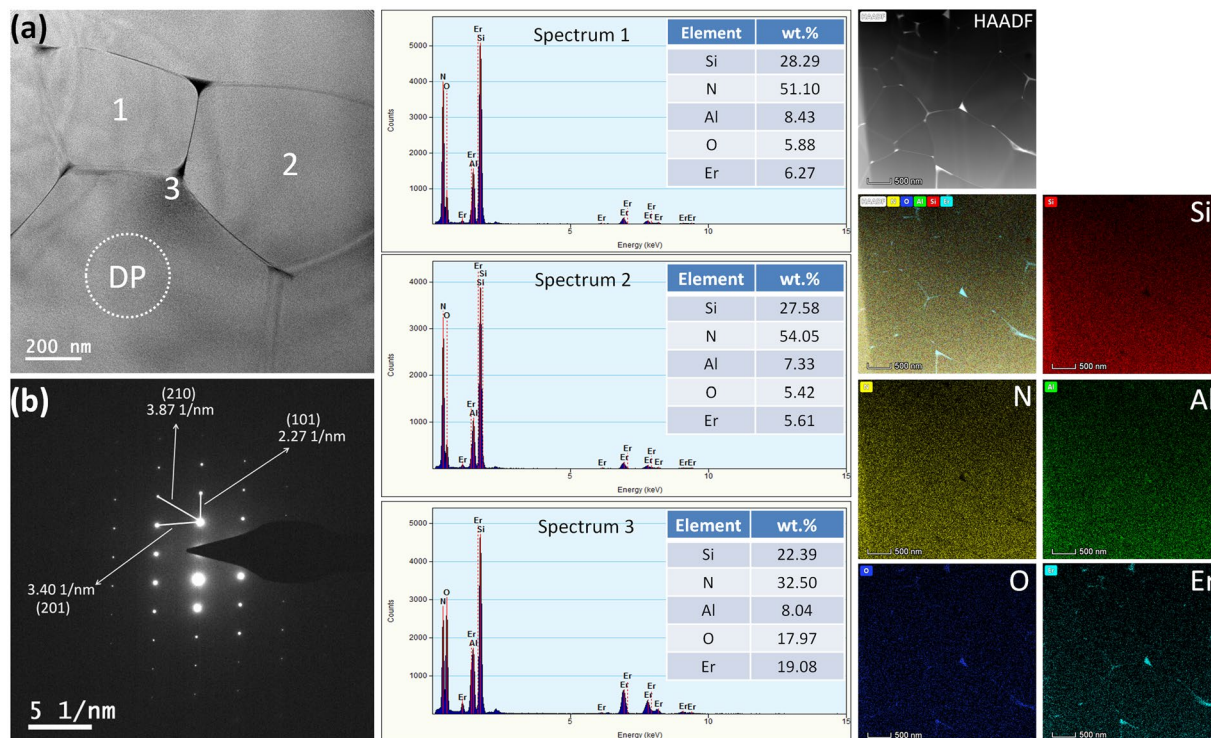
Figure 5. (**a**) TEM micrograph of the Er-α-SiAlON. (**b**) SAED pattern of the region DP in Figure (**a**). The EDS spectra 1, 2 and 3 correspond to the points marked 1, 2 and 3 in Figure (**a**). The elemental mapping diagram of Si, N, Al, O and Er correspond to the region shown in HAADF image.

through rapid non-radiative relaxations. The ESA process then excites the higher levels $^2H_{11/2}$ and $^4S_{3/2}$ giving green emissions as shown in Fig. 6(d).

The energy level $^2H_{11/2}$ can also be populated from $^4S_{3/2}$ by thermal excitation due to a very small energy gap between these two levels ($\approx 701\,cm^{-1}$) and therefore these two energy levels are called thermally coupled levels. By measuring the FIR of the two green emission peaks from $^2H_{11/2} \rightarrow {}^4I_{15/2}$ and $^4S_{3/2} \rightarrow {}^4I_{15/2}$ transitions, it is possible to use it as a probe for measuring environmental temperature where it is inserted[34]. The relative population of these thermally coupled levels of Er^{3+} follows a Boltzmann-type population distribution given by Eq. (1)[11,33,35]

$$FIR = \frac{I_{537}}{I_{558}} = \frac{N(^2H_{11/2})}{N(^4S_{3/2})} = \frac{g_H\sigma_H\omega_H}{g_S\sigma_S\omega_S}\exp\left(-\frac{\Delta E}{k_BT}\right) = C\,\exp\left(-\frac{\Delta E}{k_BT}\right) \tag{1}$$

where, N, g, σ and ω are the number of ions, the degeneracy, the emission cross-section, and the angular frequency of the radiative transitions from $^2H_{11/2}$ and $^4S_{3/2}$ to the $^4I_{15/2}$ level, respectively. ΔE is the energy gap between the $^2H_{11/2}$ and $^4S_{3/2}$ levels, k_B is the Boltzmann constant, T is the absolute temperature and $C = g_H\sigma_H\omega_H/g_S\sigma_S\omega_S$ is a constant.

Above equation can also be expressed as

$$\ln(FIR) = -\left(\frac{\Delta E}{k_B}\right)\frac{1}{T} + \ln C \tag{2}$$

Figure 7(a) shows the temperature-dependent emission spectra under 980 nm excitation in the range of 298–1373K, the highest temperature range investigated for the optical thermometry via the FIR technique. Figure 7(b) shows the FIR of the green upconversion emissions at 537 nm and 558 nm as a function of temperature under 980 nm excitation. The FIR increases from 0.164 at 298 K to 1.61 at a temperature as high as 1248 K. The FIR could be measured up to temperature 1373 K but it decreased above 1248 K because at very high temperature multiphonon decay decreases the luminescence signal. Figure 8(a) shows the linear fit of the experimental data in Eq. (2) from which we obtain the values C = 3.575 and $\Delta E = 638\,cm^{-1}$. Figure 7(c) shows the temperature-dependent emission spectra under 793 nm excitation and the corresponding FIR of the green upconversion emissions as a function of temperature is shown in Fig. 7(d). The FIR increases from 0.211 at 298 K to 2.27 at a temperature as high as 1123 K. In the case of 793 nm excitation, the FIR decreased above 1123 K because at very high temperature multiphonon decay decreases the luminescence signal. Figure 8(b) shows the linear fit of the experimental data in Eq. (2) from which we obtain the values C = 5.652 and $\Delta E = 692\,cm^{-1}$. It is emphasized that the values of ΔE obtained by the linear fit under 980 and 793 nm excitations are in very good agreement (less than 9%) with that obtained from the emission spectrum indicating that the sensor sensitivity does not vary significantly.
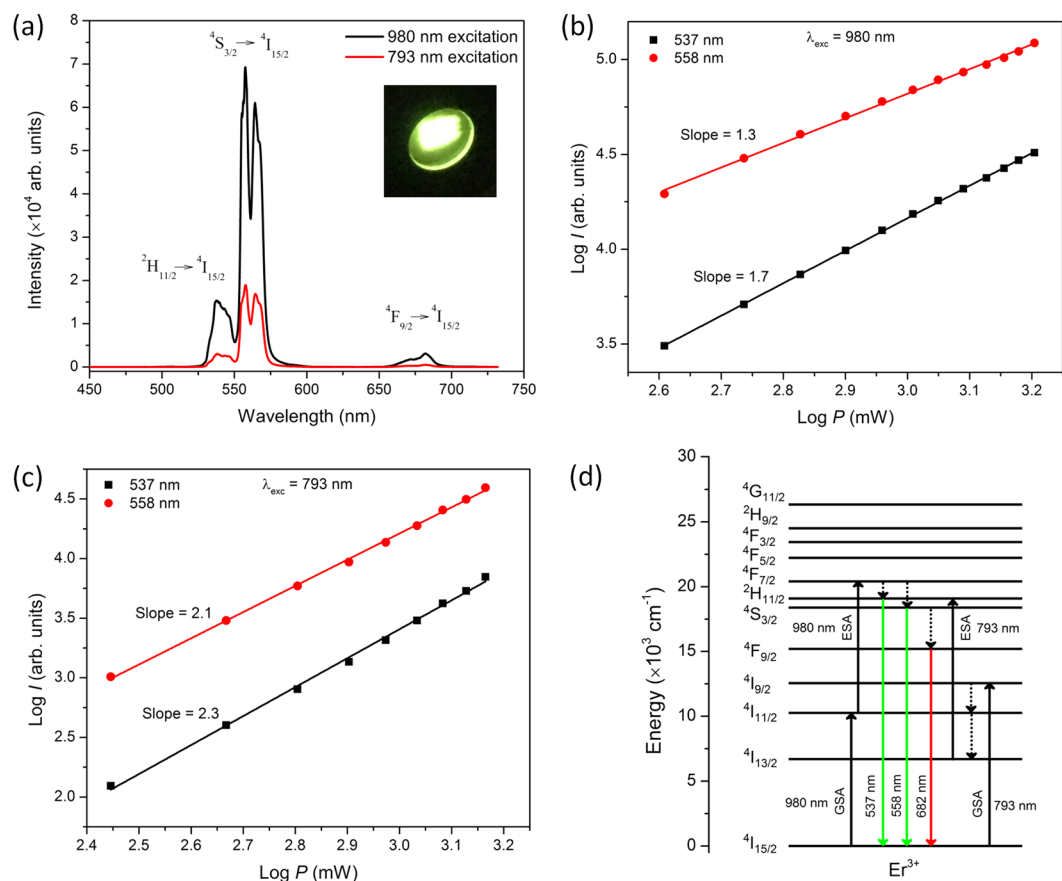
Figure 6. (**a**) Upconversion emission spectra of Er-α-SiAlON under 980 and 793 nm excitations. Inset shows the green emission photograph of Er-α-SiAlON under 980 nm excitation. (**b**) and (**c**) are pump power dependence of the emission intensity in double logarithmic representation. (**d**) Schematic energy level diagram under 980 and 793 nm excitations.

The FIR shows a high degree of linearity with respect to temperature under 793 nm excitation as compared to 980 nm excitation. Repeated experiments were carried out for the temperature-dependent emission spectra and FIR during heating and cooling cycles under 980 and 793 nm laser excitations. The results have been presented in Supplementary Fig. S3 online and Supplementary Fig. S4 online for 980 and 793 nm excitations, respectively. Under each laser excitation, it was found that the emission spectra follow identical emission patterns with only a slight change in the peak intensity during heating and cooling cycles. The FIR also shows highly consistent temperature dependency in both heating and cooling cycles. The result is the indication of high spectral stability and reproducibility of the temperature sensing behavior of Er-SiAlON ceramics.

The absolute thermal sensitivity S of the optical temperature sensing material is defined as the rate at which the FIR changes with the temperature of the host matrix[34,35] i.e.,

$$S = \frac{d(FIR)}{dT} = FIR\left(\frac{\Delta E}{k_B T^2}\right)$$

(3)

For the comparison between the sensitivities obtained for the FIR of different lanthanide ion and the host matrix combination, a relative sensitivity S_R is defined as[36].

$$S_R = \frac{1}{FIR}\frac{d(FIR)}{dT} = \frac{\Delta E}{k_B T^2}$$

(4)

Usually, absolute maximum sensitivity is employed for comparison among different host materials; however, S_R has the advantage of being independent of the nature of the thermometric technique. The plots of absolute sensitivity versus temperature under 980 and 793 nm excitations have been shown in Fig. 9. Above 1200 K, the sensitivity decreases rapidly under 793 nm excitation as compared to that under 980 nm excitation. The values of the maximum sensitivities, the temperature for the maximum sensitivity and relative sensitivity of Er-α-SiAlON along with the values for different host materials found in literature have been presented in Table 1. In the temperature range of 298–1373 K, we see that the Er-α-SiAlON ceramic shows favorable results. Er-α-SiAlON ceramic has a maximum sensitivity of 3.4×10^{-3} K^{-1} at 448 K and a relative sensitivity of 0.59% K^{-1} under 793 nm
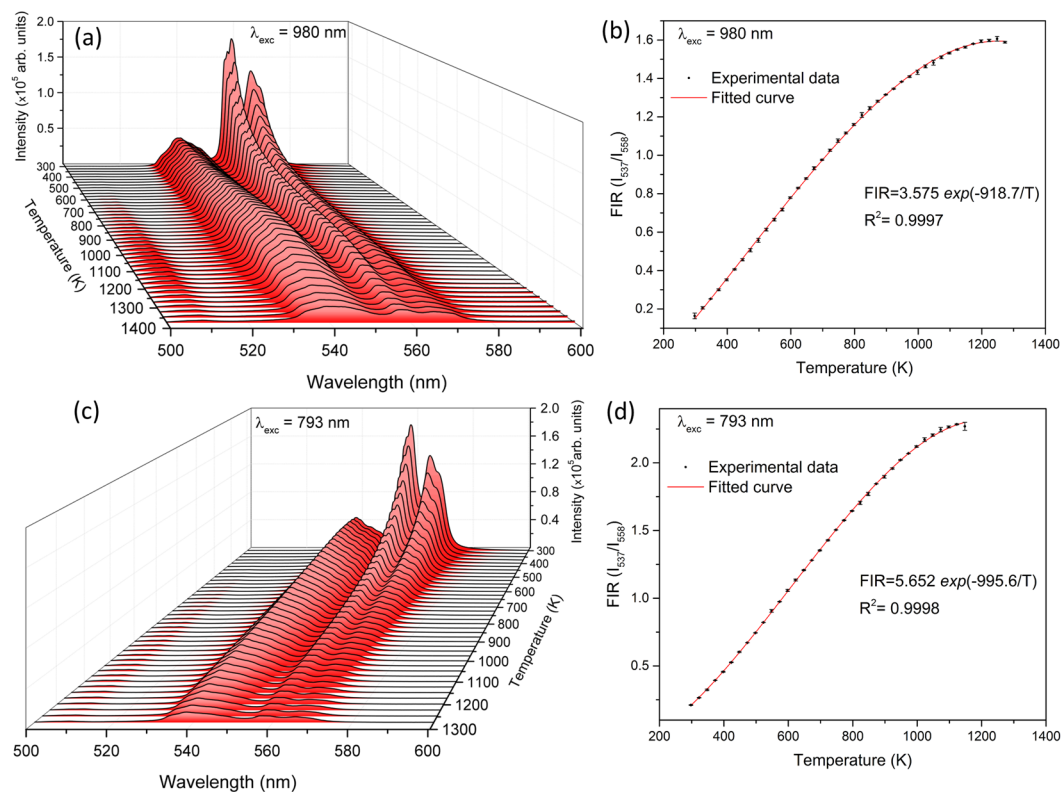
Figure 7. (**a**) Temperature-dependent emission spectra of Er-α-SiAlON under 980 nm excitation. (**b**) Plot of FIR of the two green emissions as a function of temperature in (**a**). (**c**) Temperature-dependent emission spectra of Er-α-SiAlON under 793 nm excitation. (**d**) Plot of FIR of the two green emissions as a function of temperature in (**c**).

excitation. While under 980 nm excitation, maximum sensitivity is $2.8 \times 10^{-3}\,\mathrm{K}^{-1}$ at 400 K and S_R is 0.67% K^{-1}. It is obvious that the sensitivity is not an intrinsic parameter of the sensing materials but depends on the excitation wavelength. We see that S_R is the highest for Er-α-SiAlON ceramic as compared to other hosts under 980 nm excitation as well as 793 nm excitation. Manzani *et al.* reported a high absolute sensitivity of $8.9 \times 10^{-3}\,\mathrm{K}^{-1}$ in Er/Yb-tellurite glass[11]. However, its maximum operating temperature is limited to just 473 K. Most of the works on optical thermometry via upconversion are focused on the chalcogenide[37] and fluoride[17] glasses owing to their low phonon energy. But a significant disadvantage in these materials is that their low transition temperature (T_g) severely limits the sensor operating temperature although they have higher sensitivity. It can be seen that the sensitivity of Er-α-SiAlON ceramic is better than that of Er-Silicate glass ($2.3 \times 10^{-3}\,\mathrm{K}^{-1}$ at 296 K)[38], Er-oxyfluoride glass ($2.7 \times 10^{-3}\,\mathrm{K}^{-1}$ at 543 K)[39], and it is much higher than that for Er-$\mathrm{Na_5Gd_9F_{32}}$ glass ceramics ($1.7 \times 10^{-3}\,\mathrm{K}^{-1}$ at 499 K)[40]. Even at 1273 K, it can be seen from Fig. 9 that the sensitivity of Er-α-SiAlON ceramic is about $1.0 \times 10^{-3}\,\mathrm{K}^{-1}$ under 793 nm and 980 nm excitations. This sensitivity of Er-α-SiAlON ceramic at 1273 K is still higher than the maximum sensitivity of Er-fluorozirconate glass ($0.6 \times 10^{-3}\,\mathrm{K}^{-1}$) at 300 K[13]. Dong *et al.*[41] reported optical thermometry in Er/Yb-$\mathrm{Al_2O_3}$ ceramics capable of operating at 973 K. But our results show that using Er-α-SiAlON ceramics as the sensing material, the limit of the temperature measurement via optical thermometry can be pushed beyond 1200 K, the highest temperature measurement via the FIR technique.

Temperature-dependent Raman spectra. For the application of Er-α-SiAlON ceramic as a high-temperature sensing material, understanding of its temperature-dependent phonon behavior is very essential. The comprehensive analysis of the temperature-dependent Raman spectra of Er-α-SiAlON measured for the first time over the temperature range of 298–1273 K has been presented in Fig. 10(a–c). It is found that the most intense peak at 503 cm^{-1} and the highest-phonon energy peak at 828 cm^{-1} are found to be blue-shifted (hardening behavior) in the specified temperature range. Moreover, the overall intensity of the Raman peaks also decreases with increasing temperature. The band positions versus temperatures were fitted using the following equation:

$$\omega(T) = \omega_o + \chi T \tag{5}$$

where ω_o is the frequency of vibration at absolute zero temperature and χ is the first-order temperature coefficient which is given by the slope of the fitted line. In Fig. 10(b,c), the values of χ for the peaks at 503 and 828 cm^{-1} are 0.017 and 0.016 $\mathrm{cm}^{-1}\mathrm{K}^{-1}$, respectively. The extrapolated ω_o are 498 and 822 cm^{-1} for the most intense peak and the highest-phonon energy peak respectively. Our result provides new reference data for the first-order temperature coefficients of Er-α-SiAlON ceramics. The shift of Raman frequency with respect to temperature has been
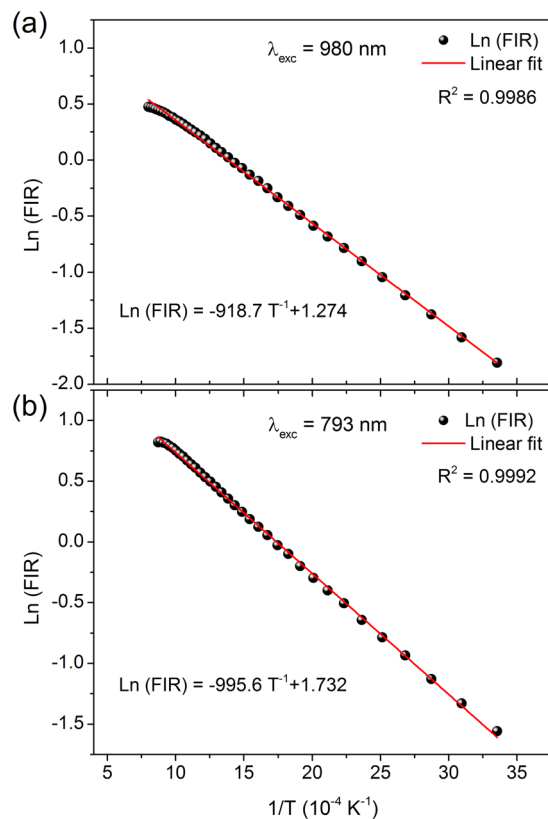
8

Figure 8. Logarithmic dependence of FIR on inverse temperature (**a**) under 980 nm excitation and (**b**) under 793 nm excitation.
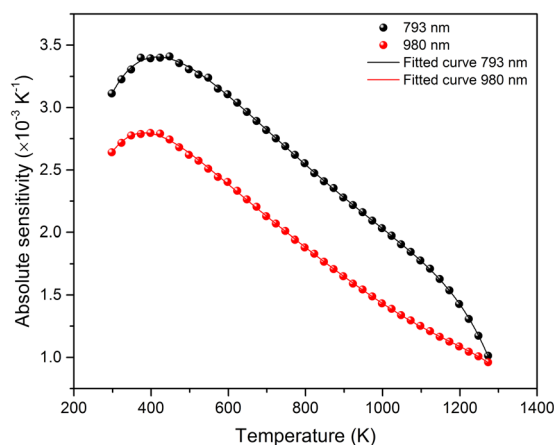

Figure 9. Absolute sensitivity versus temperature plots under 793 and 980 nm excitations.

reported in other bulk and nanomaterials[42–45] and it is the manifestation of the anharmonic term in the lattice potential energy. For each vibrational mode, the Raman shift dependence on temperature can be attributed to two reasons; the optical-phonon anharmonic coupling and the thermal expansion. The thermal expansion itself is a result of anharmonicity but it has a different physical mechanism related to the change of force constant with volume. The Raman shift direction varies for different materials, even for a given material the change in phonon frequency may differ for different vibrational modes. For example, the phonon frequencies of two of the E_g modes blue-shift while that of B_{1g} mode red-shift with the increase of temperature in anatase TiO_2[46]. Our observation of the blue- shift of the phonon frequencies in Er-α-SiAlON ceramic indicates that anharmonic couplings of the optical phonons become much stronger with increasing temperature than the contribution arising from thermal expansion. This hardening behavior might be responsible for the reduced luminescence signal observed at high temperatures (above 1248 K) in Er-α-SiAlON ceramics. A detail explanation of the hardening behavior of

Sensing materials	Maximum absolute sensitivity $(S_{max}) \times 10^{-3}\,K^{-1}$	Relative sensitivity (S_R) % K^{-1}	Temperature at maximum sensitivity K	Temperature range (K)	Excitation wavelength (nm)	Reference
Er-α-SiAlON ceramic	3.4	0.59	448	298–1273	793	This work
Er-α-SiAlON ceramic	2.8	0.67	400	298–1373	980	This work
Er-Silicate glass	2.3	—	296	296–673	978	Li et al.[38]
Er-Fluorotellurite glass	5.4	0.35	547	300–550	800	Sergio et al.[17]
Er-Fluorozirconate glass	0.6	0.58	300	150–850	805	Cai et al.[13]
Er/Yb-Al$_2$O$_3$	5.1	0.40	491	295–973	978	Dong et al.[41]
Er/Yb-tellurite glass	8.9	0.53	473	278–473	980	Manzani et al.[11]
Er-PLZT ceramic	4.0	—	556	300–883	980	Camargo et al.[14]
Er-PbO-Ga$_2$O$_3$-SiO$_2$ glass	2.6	0.24	590	296–650	980	Pisarski et al.[20]
Er/Yb-TeO$_2$-WO$_3$ glass	2.6	0.20	417	300–690	980	Pandey et al.[19]
Er-oxyfluoride glass	2.7	0.41	543	250–450	980	Feng et al.[39]
Er-fluoroindate galss	2.8	0.55	425	123–425	980	Gonzalez et al.[15]
Er-Chalcogenide glass	5.2	—	493	293–493	1060	Santos et al.[37]
Er-Na$_5$Gd$_9$F$_{32}$ glass ceramics	1.7	—	499	300–500	980	Li et al.[40]

Table 1. Comparison of the temperature sensing properties of Er-α-SiAlON ceramics with other materials.
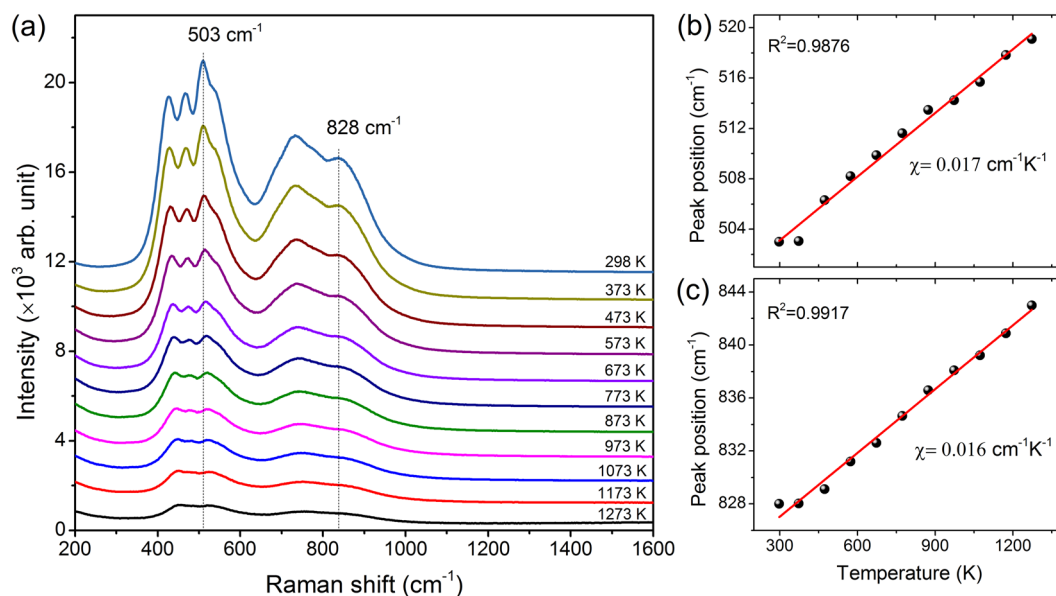

Figure 10. (**a**) Temperature-dependent Raman spectra of Er-α-SiAlON. (**b**) and (**c**) are the Raman shifts of the peaks at 503 and 828 cm^{-1}, respectively, as a function of temperature.

vibrational modes with increasing temperature in Er-α-SiAlON ceramics can be a strong motivation for further research.

Conclusion

Combining neutron diffraction, density functional theory calculations and thermodynamic modeling, we have shown that Er doping in the interstitial site of silicon nitride gives thermodynamically the most stable structure of Er-α-SiAlON. Moreover, the interstitial doping of Er is highly stabilized via chemical bonds with O-atoms with N:O ratio of 5:2 in the seven-fold coordination sites surrounding the stabilizing cation Er^{3+}. Temperature dependence of the fluorescence intensity ratio of green upconversion emission from thermally coupled energy levels $^2H_{11/2}$ and $^4S_{3/2}$ of Er^{3+} ion in Er-α-SiAlON under near-infrared excitations has been investigated for the application of this material as a high-temperature sensor. Er-α-SiAlON ceramic has a maximum sensitivity of $3.4 \times 10^{-3}\,K^{-1}$ and the relative sensitivity of 0.59% K^{-1} under 793 nm excitation while under 980 nm excitation, maximum sensitivity is $2.8 \times 10^{-3}\,K^{-1}$ and relative sensitivity is 0.67% K^{-1}. As the Er-α-SiAlON ceramic offers superior thermal and chemical stability over chalcogenide and fluoride glass-based optical temperature sensors, a maximum operating temperature of 1273 K, the highest temperature measurement via FIR technique in optical thermometry, can be achieved. We observed a blue- shift of the phonon frequencies in Er-α-SiAlON ceramic over

the temperature range of 298–1273 K indicating stronger anharmonic couplings of the optical phonons at high temperature.

Methods

Model structures.   For the simulation of thermodynamic stability and electronic structure of Er-α-SiAlON, a $1 \times 1 \times 2$ supercell of α-Si_3N_4 (space group P31c) containing 24 Si atoms and 32 N atoms was used. Both the primitive cell and the $1 \times 1 \times 2$ supercell are displayed in Fig. 1(a,b) respectively. All the drawings of the crystal structure were produced using VESTA software[47]. We took the experimentally determined geometry of Er-α-SiAlON obtained from neutron diffraction as a start point to construct the other model system. In the model structures, the Al/Si substitutions are distributed over the Si_3N_4 framework. The lanthanide ion (Er^{3+}) in α-SiAlON occupies interstitial sites of the silicon nitride structure. But, in order to investigate the thermodynamic stability, we considered Er/Si substitutions in addition to the interstitial substitution of Er^{3+}. Moreover, we considered N/O substitution as well as the interstitial substitution of O in the silicon nitride structure. One Er^{3+} cation per primitive cell of α-Si_3N_4 leads to the composition $ErSi_{9.0}Al_{3.0}N_{16.0}$ with a much higher Er-concentration than in real systems[1]. For a realistic composition, we considered one (Er^{3+} + 3Al/3Si) substitutions per $1 \times 1 \times 2$ supercell.

Calculation methods.   Density functional theory (DFT)[48,49] calculations were performed using the generalized gradient approximation (GGA), with Perdew-Burke-Ernzerhof (PBE) parameterization[50,51]. We used the Vienna *Ab initio* Simulation Package (VASP) program[52–55]. Atomic nuclei and core electrons were described by a projector-augmented wave (PAW) method. A Hubbard *U* approximation term was used to describe the strongly correlated *d* and *f*-orbitals of the Er^{3+} ions. Khon-Sham orbitals were expanded with a cutoff energy of 400 eV, and a $3 \times 3 \times 2$ and $6 \times 6 \times 4$ equally spaced *k*-point grids were employed for the Brillouin zone sampling in structural relaxations and electronic structure calculations, respectively[56]. Full relaxation of all the atomic positions was performed via a conjugate-gradient algorithm. The stopping criterion of the convergence procedure is a residual force acting on atoms smaller than 0.01 eV/A³.

Formation energies, ΔE_f of Al-, O- and Er-doping in Si_3N_4 base material are expressed as

$$\Delta E_f = E(D^q) - E_{Si_3N_4} \pm \mu_i \qquad (6)$$

where $E(D^q)$ and $E_{Si_3N_4}$ are the calculated total energies of doped and pure Si_3N_4, and μ_i is the chemical potential of species *i*. In the reactions of Al-, O- and Er-doping in Si_3N_4, the reservoirs are regarded as Al_2O_3, O_2, and Er_2O_3 because those phases are stable in our experimental conditions. The entropy terms of solid phases, Si_3N_4, Al_2O_3, and Er_2O_3 were not considered in the formation free energy calculations since the contributions of entropy to free energy are less than 0.1 eV and are mostly canceled out. For varying temperature and pressure, we express the formation energy (Eq. (6)) as a function of chemical potentials of oxygen and nitrogen,

$$\mu_O(T, P_{O_2}) = \frac{1}{2}\left\{ \widetilde{\mu}_{O_2}(T, P^\circ) + k_B T \ln\left(\frac{P_{O_2}}{P^\circ}\right) \right\} \qquad (7)$$

$$\mu_N(T, P_{O_2}) = \frac{1}{2}\left\{ \widetilde{\mu}_{N_2}(T, P^\circ) + k_B T \ln\left(\frac{P_{N_2}}{P^\circ}\right) \right\} \qquad (8)$$

where $\widetilde{\mu}_{O_2}(T, P^\circ)$ and $\{\widetilde{\mu}_{N_2}(T, P^\circ)$ are the oxygen and nitrogen chemical potential at temperature *T* and standard pressure (P°).

Materials and synthesis.   Er-α-SiAlON ceramic was prepared from high purity α-Si_3N_4 (SN-E10; UBE Co., Tokyo, Japan), AlN (Grade F; Tokuyama Co., Tokyo, Japan), Al_2O_3 (High purity chemicals Co LTD., Osaka, Japan), Er_2O_3 (High purity chemicals Co LTD., Tokyo, Japan). A single composition of Er-α-SiAlON was prepared according to the formula $M_x^{v+}Si_{12-m-n}Al_{m+n}O_nN_{16-n}$ with m = 1.5, n = 1.0. The powder preparation and the sintering technique was the same as described in our previous work[7]. The sample was sintered at 1850 °C (2123 K). The sintered samples were ground, cut and mirror-polished for various measurements.

Characterization.   The powder neutron diffraction experiment was carried out at Japan Proton Accelerator Research Complex (J-PARC), Japan, using Super High Resolution Powder Diffractometer (SuperHRPD)[57]. The measurement was done at room temperature for 24 hours. The diffraction data were used for the Rietveld refinement using Z-Rietveld software[58,59]. Microstructure and elemental analysis were carried out using transmission electron microscopy (TEM, Titan Themis Z, FEI, USA) operated at 300 kV. Photoluminescence spectra under 980 nm and 793 nm continuous wave laser (CNI lasers) excitation were recorded by Shamrock spectrograph (Shamrock 303i; Andor). For the measurement of temperature-dependent photoluminescence, Linkam thermal stage (TS1200, Linkam Scientific, UK) was home-customized and integrated with the Shamrock spectrograph. The photoluminescence spectra from 25 to 1100 °C (298 to1373 K) were measured in a step of 25 °C under ambient laboratory environment. The incident laser power was fixed at 500 mW. The heating rate was 5 °C/min and the temperature was kept constant for 10 minutes at each step to ensure correct temperature across the sample. The temperature stability was ±1 °C. Temperature-dependent Raman spectra were measured using Raman spectrometer (LabRam HR; Horiba Scientific) coupled with the same Linkam thermal stage as that was used for the temperature-dependent photoluminescence measurement. The sample was excited with 532 nm laser and the spectra were measured from 25 to 1000 °C (298 to1273 K) in an ambient laboratory environment.

References

1. Hampshire, S., Park, H. K., Thompson, D. P. & Jack, K. H. α′-Sialon ceramics. *Nature* **274**, 880–882 (1978).
2. Izumi, F., Mitomo, M. & Suzuki, J. Structure refinement of yttrium α-sialon from X-ray powder profile data. *J. Mater. Sci. Lett.* **1**, 533–535 (1982).
3. Santos, C. *et al.* Stabilization of α-SiAlONs using a rare-earth mixed oxide (RE_2O_3) as sintering additive. *Mater. Res. Bull.* **40**, 1094–1103 (2005).
4. Nishimura, T., Mitomo, M., Ishida, A. & Gu, H. Improvement of high temperature strength and creep of α-Sialon by grain boundary crystallization. *Key Eng. Mater.* **171–174**, 741–746 (2000).
5. Yamada, T., Yamao, T. & Sakata, S. Development of SiAlON -from mechanical to optical applications-. *Key Eng. Mater.* **352**, 173–178 (2007).
6. Xie, R. J., Hirosaki, N., Sakuma, K., Yamamoto, Y. & Mitomo, M. Eu^{2+}-doped Ca-α-SiAlON: A yellow phosphor for white light-emitting diodes. *Appl. Phys. Lett.* **84**, 5404–5406 (2004).
7. Kshetri, Y. K., Joshi, B., Diaz-Torres, L. A. & Lee, S. W. Efficient near infrared to visible and near-infrared upconversion emissions in transparent (Tm^{3+}, Er^{3+})-α-Sialon ceramics. *J. Am. Ceram. Soc.* **100**, 224–234 (2017).
8. Kshetri, Y. K., Joshi, B. & Lee, S. W. Intense visible upconversion emission in transparent (Ho^{3+}, Er^{3+})-α-Sialon ceramics under 980nm laser excitation. *J. Eur. Ceram. Soc.* **36**, 4215–4224 (2016).
9. Li, B. *et al.* Upconversion luminescence properties of Er^{3+}/Yb^{3+} in transparent α-Sialon ceramics. *Opt. Mater. (Amst).* **39**, 239–246 (2015).
10. Da Cunha, M. P., Moonlight, T., Lad, R., Frankel, D. & Bernhardt, G. High temperature sensing technology for applications up To 1000 °C. *Proc. IEEE Sensors* 752–755, https://doi.org/10.1109/ICSENS.2008.4716550 (2008).
11. Manzani, D. *et al.* A portable luminescent thermometer based on green up-conversion emission of Er^{3+}/Yb^{3+} co-doped tellurite glass. *Sci. Rep.* **7**, 41596 (2017).
12. Chai, X., Li, J., Wang, X., Li, Y. & Yao, X. Color-tunable upconversion photoluminescence and highly performed optical temperature sensing in Er^{3+}/Yb^{3+} co-doped $ZnWO_4$. *Opt. Express* **24**, 22438 (2016).
13. Cai, Z. P. & Xu, H. Y. Point temperature sensor based on green upconversion emission in an Er:ZBLALiP microsphere. *Sensors Actuators, A Phys.* **108**, 187–192 (2003).
14. De Camargo, A. S. S. *et al.* Infrared to visible frequency upconversion temperature sensor based on Er^{3+}-doped PLZT transparent ceramics. *Solid State Commun.* **137**, 1–5 (2006).
15. Haro-González, P., León-Luis, S. F., González-Pérez, S. & Martín, I. R. Analysis of Er^{3+} and Ho^{3+} codoped fluoroindate glasses as wide range temperature sensor. *Mater. Res. Bull.* **46**, 1051–1054 (2011).
16. Alencar, M. A. R. C., Maciel, G. S., de Araújo, C. B. & Patra, A. Er^{3+}-doped $BaTiO_3$ nanocrystals for thermometry: Influence of nanoenvironment on the sensitivity of a fluorescence based temperature sensor. *Appl. Phys. Lett.* **84**, 4753–4755 (2004).
17. León-Luis, S. F., Rodríguez-Mendoza, U. R., Lalla, E. & Lavín, V. Temperature sensor based on the Er^{3+} green upconverted emission in a fluorotellurite glass. *Sensors Actuators, B Chem.* **158**, 208–213 (2011).
18. Wawrzynczyk, D., Bednarkiewicz, A., Nyk, M., Strek, W. & Samoc, M. Neodymium(iii) doped fluoride nanoparticles as non-contact optical temperature sensors. *Nanoscale* **4**, 6959–6961 (2012).
19. Pandey, A. *et al.* Enhanced upconversion and temperature sensing study of Er^{3+}-Yb^{3+} codoped tungsten-tellurite glass. *Sensors Actuators, B Chem.* **202**, 1305–1312 (2014).
20. Pisarski, W. A., Pisarska, J., Lisiecki, R. & Ryba-Romanowski, W. Sensitive optical temperature sensor based on up-conversion luminescence spectra of Er^{3+} ions in $PbO–Ga_2O_3–XO_2$ (X = Ge, Si) glasses. *Opt. Mater. (Amst).* **59**, 87–90 (2016).
21. Fang, C. M. & Metselaar, R. First-principles calculations of the stability and local structure of α-sialon ceramics on the line Si_3N_4 −½Ca_3N_2:3AlN. *J. Phys. Condens. Matter* **16**, 2931 (2004).
22. Benco, L., Hafner, J., Lences, Z. & Sajgalik, P. Density functional study of structures and mechanical properties of Y-doped α-SiAlONs. *J. Eur. Ceram. Soc.* **28**, 995–1002 (2008).
23. Zhong, H. M., Liu, Q., Jiang, J., Sun, G. Y. & Luo, Y. A first principles study on optical transparency mechanism in Dy doped α-SiAlON ceramics. *J. Appl. Phys.* **106**, 104–107 (2009).
24. Cole, M., O'Reilly, K. P. J., Redington, M. & Hampshire, S. EXAFS study of a hot-pressed α'-sialon ceramic containing erbium as the modifying cation. *J. Mater. Sci.* **26**, 5143–5148 (1991).
25. Izumi, F., Mitomo, M. & Bando, Y. Rietveld refinements for calcium and yttrium containing α-sialons. *J. Mater. Sci.* **19**, 3115–3120 (1984).
26. Cao, G. Z., Metselaar, R. & Haije, W. G. Neutron diffraction study of yttrium α'-sialon. *J. Mater. Sci. Lett.* **12**, 459–460 (1993).
27. Van Krevel, J. W. H., Van Rutten, J. W. T., Mandal, H., Hintzen, H. T. & Metselaar, R. Luminescence properties of Terbium-, Cerium-, or Europium-doped α-Sialon materials. *J. Solid State Chem.* **165**, 19–24 (2002).
28. Goodman, A. M. Photoemission of electrons and holes into silicon nitride. *Appl. Phys. Lett.* **13**, 275–277 (1968).
29. Kresse, G., Marsman, M., Hintzsche, L. E. & Flage-Larsen, E. Optical and electronic properties of Si_3N_4 and α-SiO_2. *Phys. Rev. B* **85**, 045205 (2012).
30. Pollnau, M., Gamelin, D., Lüthi, S., Güdel, H. & Hehlen, M. Power dependence of upconversion luminescence in lanthanide and transition-metal-ion systems. *Phys. Rev. B* **61**, 3337–3346 (2000).
31. Hehlen, M., Cockroft, N., Gosnell, T. & Bruce, A. Spectroscopic properties of Er^{3+}- and Yb^{3+}-doped soda-lime silicate and aluminosilicate glasses. *Phys. Rev. B* **56**, 9302–9318 (1997).
32. Tsuda, M., Soga, K., Inoue, H., Inoue, S. & Makishima, A. Upconversion mechanism in Er^{3+}-doped fluorozirconate glasses under 800 nm excitation. *J. Appl. Phys.* **85**, 29–37 (1999).
33. Maurice, E., Monnom, G., Ostrowsky, D. B. & Baxter, G. W. High dynamic range temperature point sensor using green fluorescence intensity ratio in erbium-doped silica fiber. *J. Light. Technol.* **13**, 1349–1353 (1995).
34. Wade, S. A., Collins, S. F. & Baxter, G. W. Fluorescence intensity ratio technique for optical fiber point temperature sensing. *J. Appl. Phys.* **94**, 4743–4756 (2003).
35. Collins, S. F. *et al.* Comparison of fluorescence-based temperature sensor schemes: Theoretical analysis and experimental validation. *J. Appl. Phys.* **84**, 4649–4654 (1998).
36. Wade, S. A. Temperature Measurement Using Rare Earth Doped Fibre Fluorescence. PhD thesis, *Victoria University, Melbourne, Australia* (1999).
37. Dos Santos, P. V., De Araujo, M. T., Gouveia-Neto, A. S., Medeiros Neto, J. A. & Sombra, A. S. B. Optical thermometry through infrared excited upconversion fluorescence emission in Er^{3+}-and Er^{3+}-Yb^{3+}-doped chalcogenide glasses. *IEEE J. Quantum Electron.* **35**, 395–399 (1999).
38. Li, C., Dong, B., Ming, C. & Lei, M. Application to temperature sensor based on green up-conversion of Er^{3+} doped silicate glass. *Sensors* **7**, 2652–2659 (2007).
39. Feng, L., Lai, B., Wang, J., Du, G. & Su, Q. Spectroscopic properties of Er^{3+} in a oxyfluoride glass and upconversion and temperature sensor behaviour of Er^{3+}/Yb^{3+}-codoped oxyfluoride glass. *J. Lumin.* **130**, 2418–2423 (2010).

40. Li, X., Cao, J., Hu, F., Wei, R. & Guo, H. Transparent $Na_5Gd_9F_{32}$:Er^{3+} glass-ceramics: enhanced up-conversion luminescence and applications in optical temperature sensors. *RSC Adv.* **7**, 35147–35153 (2017).
41. Dong, B. *et al.* Optical thermometry through infrared excited green upconversion emissions in Er^{3+}-Yb^{3+} codoped Al_2O_3. *Appl. Phys. Lett.* **90**, 3–6 (2007).
42. Calizo, I., Balandin, A. A., Bao, W., Miao, F. & Lau, C. N. Temperature dependence of the Raman spectra of graphene and graphene multilayers. *Nano Lett.* **7**, 2645–2649 (2007).
43. Zhang, Y. *et al.* Raman study of 2D anatase TiO_2 nanosheets. *Phys. Chem. Chem. Phys.* **18**, 32178–32184 (2016).
44. Huang, X. *et al.* Quantitative analysis of temperature dependence of Raman shift of monolayer WS_2. *Sci. Rep.* **6**, 1–8 (2016).
45. Sun, H. Y. *et al.* Temperature dependence of Raman scattering in bulk 4H-SiC with different carrier concentration. *Opt. Express* **21**, 26475 (2013).
46. Sahoo, S., Arora, A. K. & Sridharan, V. Raman line shapes of optical phonons of different symmetries in anatase TiO_2 nanocrystals. *J. Phys. Chem. C* **113**, 16927–16933 (2009).
47. Momma, K. & Izumi, F. VESTA 3 for three-dimensional visualization of crystal, volumetric and morphology data. *J. Appl. Crystallogr.* **44**, 1272–1276 (2011).
48. Hohenberg, P. & Kohn, W. Inhomogeneous electron gas. *Phys. Rev. B* **136**, 1912–1919 (1964).
49. Kohn, W. & Sham, L. J. Self-consistent equations including exchange and correlation effects. *Phys. Rev.* **140**, A1133–1138 (1965).
50. Perdew, J. P., Burke, K. & Ernzerhof, M. Generalized gradient approximation made simple. *Phys. Rev. Lett.* **77**, 3865–3868 (1996).
51. Perdew, J. *et al.* Atoms, molecules, solids, and surfaces: Applications of the generalized gradient approximation for exchange and correlation. *Phys. Rev. B.* **46**, 4978–4978 (1992).
52. Kresse, G. & Hafner, J. *Ab initio* molecular dynamics for liquid metals. *Phys. Rev. B.* **47**, 558–561 (1993).
53. Kresse, G. & Hafner, J. *Ab initio* molecular-dynamics simulation of the liquid-metal–amorphous-semiconductor transition in germanium. *Phys. Rev. B.* **49**, 14251–14269 (1994).
54. Kresse, G. & Furthmüller, J. Efficiency of ab-initio total energy calculations for metals and semiconductors using a plane-wave basis set. *Comput. Mater. Sci.* **6**, 15–50 (1996).
55. Kresse, G. & Furthmüller, J. Efficient iterative schemes for *ab initio* total-energy calculations using a plane-wave basis set. *Phys. Rev. B* **54**, 11169–11186 (1996).
56. Monkhorst, H. J. & Pack, J. D. Special points for Brillouin-zone integrations. *Phys. Rev. B* **13**, 1748–1749 (1976).
57. Torii, S. *et al.* Super High resolution powder diffractometer at J-PARC. *J. Phys. Soc. Japan* **80**, 3–6 (2011).
58. Oishi, R. *et al.* Rietveld analysis software for J-PARC. *Nucl. Instruments Methods Phys. Res. A* **600**, 94–96 (2009).
59. Oishi-Tomiyasu, R., Yonemura, M. & Morishima, T. Application of matrix decomposition algorithms for singular matrices to the Pawley method in Z-Rietveld. *J. Appl. Crystallogr.* **45**, 299–308 (2012).

Acknowledgements

Author contributions

Y.K. Kshetri developed the concept, designed and performed experiment, analyzed data and wrote the manuscript. T. Kamiyama and S. Torii performed neutron diffraction experiment and analyzed the data. S.H. Jeong and T.-H. Kim managed the project administration and resources. Y.K. Kshetri and H. Choi performed DFT calculations. J. Zhou and Y.P. Feng contributed with the data analysis and discussions of DFT calculations. Y.K. Kshetri and S.W. Lee secured the funding. S.W. Lee supervised the work. All the authors discussed the results and reviewed the manuscript.

Competing interests

The authors declare no competing interests.

Additional information

Supplementary information is available for this paper at https://doi.org/10.1038/s41598-020-61105-z.

Correspondence and requests for materials should be addressed to Y.K.K. or S.W.L.

Reprints and permissions information is available at www.nature.com/reprints.

Publisher's note Springer Nature remains neutral with regard to jurisdictional claims in published maps and institutional affiliations.